Intra-night flickering of T Coronae Borealis: Flickering parameters and quasi-period modes. Comparison with RS Ophiuchi

Ts. B. Georgiev, S. Boeva, G. Latev,
E. Semkov, K. A. Stoyanov, S. V. Tsvetkova
Institute of Astronomy and National Astronomical Observatory,
Bulgarian Academy of Sciences, 72 Tsarigradsko Chaussee Blvd., 1784 Sofia, Bulgaria
tsgeorg@astro.bas.bg
(Submitted on 25.01.2020. Accepted on 20.07.2020)

Abstract. We analyze 40 U-band light curves (LCs) of the flickering source (FS) of the symbiotic recurrent nova T CrB, observed over 1993–2018. The light contribution of the red giant is removed. The LCs are linearized, flattened and processed by a method, created earlier for the case of RS Oph. The method is described and results for T CrB and RS Oph are compared.

Over the period 2009–2017 the average flux of the FS increased by 2.5 mag or 10.1 times. Simultaneously, the standard deviation and amplitude deviation of the LC increased about 2.7 and 3.7 times, respectively, which is an evidence that the average and scatter of the flickering are connected.

The statistics of the skewness, kurtosis, structure gradient and Hurst gradient of the LCs of T CrB are similar to these of RS Oph, giving a hint that the flickering of T CrB contains larger fraction of single shots. This fraction increases toward the short time scale of the flickering. In comparison with a Gaussian distribution, the FS of T CrB shows some excess of large positive deviations while FS of RS Oph shows some deficit of short deviations.

As in the case of RS Oph, all LCs of T CrB show time structures, sometimes repeatings, with quasi-periods (QPs) from minutes to tens of minutes. Using the minima of the structure function and the maxima of the auto-correlation function we detected 84 QPs – 48 in 40 whole LCs and 36 in 32 partial high resolution LCs. The distribution of the revealed QPs shows modes at 4.7, 11.8, 19.0, 42.1 and 81.7 min. The QP modes of T CrB and RS Oph follow the power functions $QP_M = 5.1 \times 2.0^M$ and $QP_M = 3.47 \times 1.55^M$, respectively, where M is the mode number. It seems that these power functions describe regularities corresponding to 2:1 and 3:2 resonances, with unknown reason.

Key words: stars: binaries: symbiotic – novae, cataclysmic variables – accretion, accretion discs – stars: individual: T CrB, RS Oph.

Introduction

T CrB is a symbiotic binary star and recurrent nova. It contains an M3 III type red giant (Shenavrin, Taranova & Nadzhip 2011) with mass 0.6 $M_\odot$ and a carbon-oxygen white dwarf with mass 1.2 $M_\odot$ and luminosity 40 $L_\odot$ (Iłkiewicz et al. 2016). The orbit of the system is circular with period 226 d (Fekel et al. 2000) and inclination 67° (Stanishev et al. 2004).

Zamanov et al. (2004, Paper I) analyzed 27 electro-photometric light curves (LCs) of T CrB. After subtraction of the contribution of the red giant they found that the flickering amplitude of the flickering source (FS) correlates with the average flux. They found also that from this point of view the flickering of the FS of T CrB is more stable in comparison with the jet-ejecting symbiotic stars CH Cyg and MWC 560.

The flickering parameters of the symbiotic stars vary over scales of minutes, hours, days, etc. The study of the physics of the flickering requires at least (i) deriving of parameters of the flickering at different time scales

and (ii) revealing of quasi-periods (QPs) and morphologies of the repeating details. Such information from the apparent chaos of the flickering LC may be extracted by specific statistical and fractal methods. This approach is preferable because (i) it is conceptually simple, (ii) it is weakly sensitive to non-equality of the data sampling and (iii) in contrast with the Fourier method it is well applicable at low signal-to-noise ratio.

Such approach has been applied by Georgiev et al. (2020a, Paper II) for analysis of the flickering of the symbiotic recurrent nova RS Oph. The main result is the deriving of 8 QP modes, at 3.5, 5.3, 8, 13, 21, 30, 48 and 73 min. This series obeys a regularity (near-commensurability) corresponding to a power function with base $1.55 \approx 3/2$ (Georgiev et al. 2020b, Paper III).

The purposes of the present paper are (i) to give description of the method, (ii) to show the photometric behavior of the FS over the years, (iii) to characterize the flickering by various parameters, (iv) to reveal flickering QPs and their modes, as well as (v) to compare the results for T CrB and RS Oph.

The contents follows:

Input data and numerical results of the processing are presented in the Tables in Appendix A. Details of the method are presented in Fig. 1 and Fig. 2, as well as, by the same manner, in the panels with graphs in Appendixes B and C. The Appendixes A, B and C are Supplement material, available only in the electronic version of the article in the Bulgarian Astronomical Journal.

The used abbreviations and subscripts follow:

ACF – auto-correlation function (Eq. 7, Fig. 1(f));
AF – asymmetry (ratio) function (EQ. 6, Fig. 1(e));
AV – average value;
BH – bin of histogram;
BT – breakdown time point of the AF (Fig. 1(e));
CC – coefficient of correlation;
DF – (standard) deviation function (Eq. 3, Fig. 1(d));
FS – flickering source;
HF, HG – Hurst function, Hurst gradient (Eq. 5, Fig. 1(e));
GR – gradient of the regression (slope coefficient);
LC – light curve (Eq. 1, 2; Fig. 1(a), 1(b));
MLS – method of the least squares;
QP – quasi-period in the LC (Fig. 1(d), 1(f));
RD, RF – range deviation, range function (Eq. 3);
SD – standard deviation.
RRLC – relative residual light curve (Eq. 2, Fig. 1(c));

SF, SG – structure function, structure gradient (Eq. 4, Fig. 1(d)).

1. Observations and data processing

The basic data about the observational material are collected in the on-line Appendix A, Table 1.

The first part of the observational data contains 27 electro-photometric LCs, #01–#27, taken with the 60 cm Cassegrain telescope at+ the Rozhen NAO in 1993–1999. The monitoring durations are $T_{\rm M} = 20 - 189$ min (average 85 ± 45 min), the number of data points from a single run is $n_{\rm M} = 96 - 674$ (average 386 ± 144) with integration time 5, 10 or 20 s. The photometric standard error is about 0.03 mag. These 27 LCs are analyzed also in Paper I.

The second part of the observational data contains 13 CCD LCs, #28–#40, taken by the 2 m RCC telescope, the 60 cm Cassegrain telescope and the 50/70 cm Schmidt telescope at the Rozhen NAO in 2000–2018. The monitoring durations are $T_{\rm M} = 66 - 185$ min (average 85 ± 45 min), the number of CCD frames in a single run is $n_{\rm M} = 24 - 191$ (average 85 ± 54) and the time step (time resolution) is $\tau_{\rm M} = 1 - 4$ min (average 2 ± 1.3 min). The photometric standard error is about 0.01 mag.

Additionally we detached 32 short parts from high resolution electro-photometric LCs. We consider them as separate single LCs and used them mainly for detection of short QPs. The results from the analysis of our 40 + 32 = 72 LCs are collected in Appendix A.

The graphs in Fig. 1 and Fig. 2 illustrate the processing stages, developed in Paper II. Galleries of such graphs are collected in Appendixes B, for 40 basic LCs and in Appendix C, for 32 additionally extracted parts of LCs. The LC #01, shown in Fig. 1(a), is the most difficult case where the monitoring is interrupted at least 6 times by atmospheric conditions. Three parts of #01 are analyzed and shown in the beginning of Appendix C as #01a, #01b and #01c. The LC #03a, regarded in Fig. 2, is the shortest part LC. The respective full LC #03 is presented in Appendix B.

1.1. Light curves and parameters

Convenient statistical parameters may be used for revealing of numerous properties of the LCs. We are forced to provide 4 kinds of LCs – magnitude, linearized, residual (flatten) linearized and relative residual linearized. The relevant graphs of the linearized and the relative residual linearized LCs are presented in sub-figures (a) and (b) in Fig. 1 and 2, as well as in the respective figures in Appendix B and C. We deal mainly with the last of them, relative residual LC ($u(t)$, Eq. 2), expressed by percents.

Linearized LCs of the FS are necessary for correct and uniform trend removal, statistical analysis and QP detection. First the magnitude LCs of the system T CrB were reduced to LCs of the FS only by removal of the contribution of the red giant with $U_0 = 13.75$ mag and account for extinction of $E_{B-V} = 0.15$ (Paper I). Further the result is linearized, i.e.

converted from magnitudes U into fluxes u by means of the definition of stellar magnitude:

$$u(t) = u_0 \times \mathrm{dex}[-0.4 \times (U(t) - U_0)]. \quad (1)$$

Accepting a flux of $u_0 = 4.194 \times 10^{-11}$ W m^{-2} min^{-1} for magnitude $U_0 = 0$ (Bessel 1979) we derive linearized LCs of the FS in units of 10^{-16} W m^{-2} min^{-1}.

If the LC is a time series of a stationary physical flickering, it may be well characterized by its average value (AV), u_{AV}, standard deviation (SD), u_{SD} (in respect to the AV), range deviation (RD) u_{RD} (in this paper – the half of the peak-to-peak amplitude), etc. But the LC contains at least 3 variable components.

The first component, observable on the sub-minute and minute scale is the photometric noise. We consider that component to be faint enough and it is not a subject of this work. The second one, observable on the multi-minute scale, is the subject for QPs search under our observing circumstances. The third component is observable on the multi-hour scale. It presents in our time bounded LC occasionally and fragmentarily. It is obstructive for QP detection and it ought to be removed or suppressed. Therefore, the linearized LCs must be flattened, i. e. converted into residual LCs, by removal of their large scale trends. Then the result will be obligatory for applying of the structure function and auto-correlation function as QP detectors in the minute and multi-minute scale. (See below.)

In Paper II and here we fit the large scale trend of the whole linearized LC by a low degree polynomial and remove its values from the LC. A better but technically difficult approach may be a sliding local flattening by a suitable robust fitting. Such an approach needs a choice of specific robust method and development of suitable smoothing strategy. This may be a subject of another work.

Figures 1(a) and 2(a) show linearized LCs ($u(t)$, Eq. 1) from the monitoring #01 and #03a. The numbers of of data n_{M} are 448 and 39, respectively. The degrees m of their fitting polynomials are 4 and 0. The levels of the average (AV) fluxes are drown by horizontal dashed lines.

Residual LCs $\Delta u(t)$ and relative residual LCs (RRLCs) $\delta u(t)$ are necessary for uniform and mutually compatible presentation of various parameters. Their forms are

$$\Delta u(t) = u(t) - u^{(m)}(t) \quad \text{and} \quad \delta u(t) = \Delta u(t)/u^{(m)}(t), \quad (2)$$

where $u^{(m)}(t)$ is a m-th degree fitting polynomial. These LCs have zero averages, $\Delta u_{\mathrm{AV}} = \delta u_{\mathrm{AV}} = 0$, but they are characterized by specific SDs Δu_{SD}, δu_{SD} and RDs Δu_{RD}, δu_{RD}, etc.

The polynomial degree is adopted to ensure almost identical QPs detected by the structure function and autocorrelation function (see below). Special example about the influence of the polynomial degrees 1, 3, 5 or 7 on the results is given in Paper II, Fig. 6. The polynomial degrees and the numbers of their applications in this work are: 0-3, 1-3, 2-23, 3-24, 4-10, 5-8, 7-1 (Appendix A). The average decrease of the SD of the linearized

LCs after trend removal is 1.5 ± 0.3 times (up to 2 times, 3 times only for #20a). In the case of RS Oph we have 1.7 ± 0.8 times (up to 5.7 times). The reason is that at RS Oph the large scale light variations are larger and at T CrB the photometric noise is larger.

Figure 1(b) and 2(b) show the RRLCs ($\delta u(t)$, Eq. 2). The horizontal dashed lines show the levels of AV and AV ± SDs. The monitoring times $T_{\rm M}$ are 121 and 7 min. The average time resolutions $\tau_{\rm M} = T_{\rm M}/n_{\rm M}$ are 0.27 and 0.18 min, respectively. For compatibility our RRLCs are expressed in percents in respect to the relevant values of the fitting polynomial. Thus various kinds of time series may be easily compared with the stellar flickering (Paper II).

Some of the RRLCs show eruptions without clear peak, with amplitudes about 20% and with duration 10–15 min. Such are the LCs # # 09, 10, 12, 14, 18, 23, 31 (Appendix B).

The histogram (distribution) $\eta(\delta u)$ of the RRLC (sub-figures (b)) is characterized by the scatter parameters SD and RD, and the shape parameters skewness (asymmetry, A') and kurtosis (exes, E'). We derive these parameters by the formulae for data samples found by Joanes & Gill (1998; See Paper II).

A Gaussian-like distribution poses $A' \approx E' \approx 0$. A value of $A' > 0$ corresponds to a larger right tail of the histogram, i. e. to an excess of positive large deviations (and vice versa). A value of $E' > 0$ corresponds histogram with a higher central part in combination with large wings. This is an evidence of some excess of both small and large deviations (and vice versa).

Figures 1(c) and 2(c) present the histograms $\eta(\delta u)$ from the RRLCs in Fig. 1(b) and 2(b), as well as their skewness A', kurtosis E' and buns of histograms BH. The position of the apex of the triangle under the histogram shows the median value of the distribution. The base of the triangle is the median error bar, which covers 68% of the distributed data. All histograms in this paper are smoothed slightly for better visualizing by convolution kernel [0.25, 0.50, 0.25].

The histograms of the RRLC in Fig. 1(c) and 2(c) have no significant skewness, i.e. the distributions of the deviations of the RRLC are approximately symmetric. But the negative kurtosis in Fig. 1(c) gives evidence about some general deficit of very short and very large deviations. Such a fact is remarked also in some LCs of RS Oph (Paper II). A particular reason for low kurtosis may be the complicated large scale trend of the RRLC which is not well fitted in Fig.1(a). In Fig. 2(a) the skewness is not so negative, the variations of the brightness avoid the zero level and the histogram is even bifurcated.

It is clear that even in the case of a Gaussian distribution of the RRLC around some large scale trend, the adopted (insufficiently flexible) polynomial fit is able to change the scatter, i. e. the shape of the histogram. Therefore, a single histogram may not be a good representative. Histogram parameters of numerous RRLCs are necessary to suppress the polynomial effects. Generally, more sophisticated method for deriving of RRLCs is need.

The statistics of the shape parameters A' and E' for our 72 RRLCs

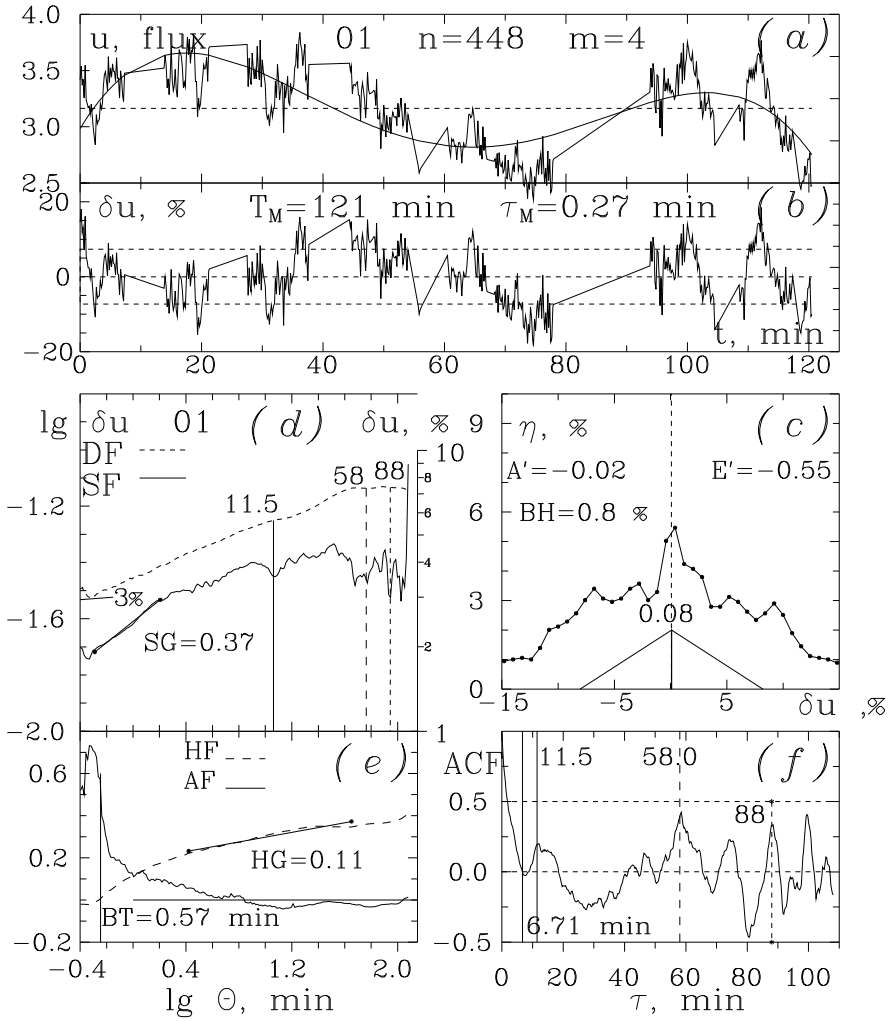

Fig. 1. LC #01. **(a)**: Linearized LC (Eq. 1) with n points, fitted by a polynomial of degree m; **(b)**: RRLC (Eq. 2) with duration $T_{\rm M}$ and average time resolution $\tau_{\rm M}$; **(c)**: Histogram of the RRLC (b) with bin size BH, skewness A', kurtosis E', median (position of the triangle apex) and 34% median deviation (the half of the triangle base); **(d)**: Density function DF (Eq. 3) with estimation of the photometric noise (the level of the initial minimum, here 3%) and structure function SF (Eq. 4) with structure gradient SG and detected QPs (positions of the minima, marked by verticals); **(e)**: Hurst function HF (Eq. 5) with Hurst gradient HG and asymmetry function AF (Eq. 6) with breakdown time point(BT); **(f)** Auto-correlation function ACF (Eq. 7) with confirmed QPs (position of the maxima, marked by verticals).

are shown in Fig. 5. The median values are 24 ± 0.32 and 0.02 ± 0.44, respectively.

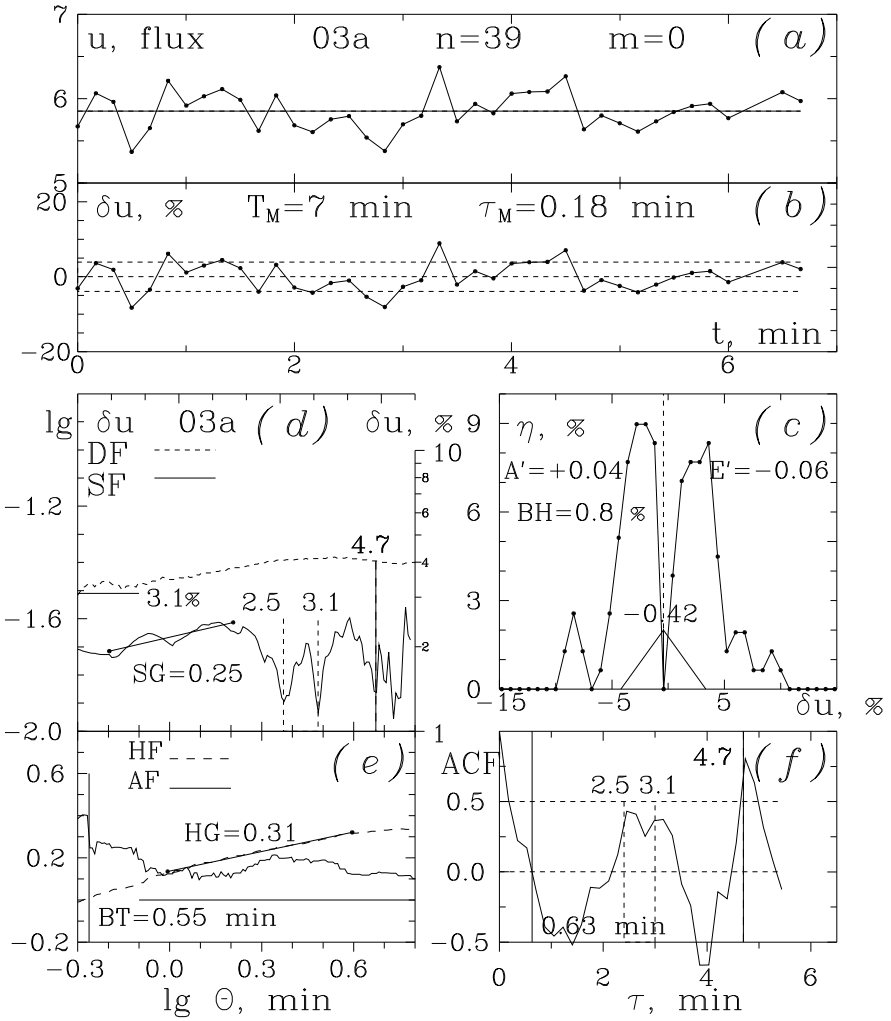

Fig. 2. LC #03a. **(a)**: Linearized LC; **(b)**: RRLC; **(c)**: Histogram of the RRLC (b); **(d)**: SF, DF and detected QPs; **(e)**: HF, AF and BT; **(f)**: ACF and confirmed QPs. See for details Fig. 1.

1.2. Fractal functions and parameters

Some useful (fractal) functions, defined on the RRLC (Eq. 2) and presented in log-log coordinates are used for revealing of specific properties of the RRLCs. Following the recommendations of Mandelbrot (1982), Russ (1994), Hastings & Sugihara (1995), Falkoner (1997), we use the simplest 3 fractal methods, characterizing the "roughness" and "jaggedness" (Eq. 3), as well as the "periodicity" of the RRLs (Eq. 4). The relevant graphs are

presented in sub-figures (d) and (e) in Fig. 1, Fig. 2 and figures in Appendix B and C.

This study of a discrete RRLC $\delta u(t_n), n = 1, 2, ..., N$ is based on a system of scanning data windows with time sizes $\Theta_j, j = 1, 2, ..., J$, e. g. $J = 99$. The window sizes are distributed uniformly by lg Θ. Each j-th window scans the RRLC, taking $k = 1, 2, ..., K$ different positions. The k-th position of the j-th window gives, e. g., fractal indicators of scatter, $\delta u_{\rm SD}(\Theta_k)_j$, $\delta u_{\rm RD}(\Theta_k)_j$. The value of each such indicator, averaged over all K positions of the j-th window, gives relevant fractal parameter of scatter, $< \delta u_{\rm SD}(\Theta) >_j$, $< \delta u_{\rm SD}(\Theta) >_j$. Hereafter the broken brackets mean averaging for all k positions of the window with size Θ_j in the RRLC.

The dependence of each similar parameter on its window size, in log-log coordinates, is considered as fractal function. Suitable indicators and parameters are used for the definition of the functions in Eqs. 3, 4, 5, 6 and 7.

The (standard) deviation function (DF) and the range deviation function (RF) describe the increase of the RRLC scatter parameters

$$DF_j(\Theta) =< \delta u_{\rm SD}(\Theta) >_j, \qquad RF_j(\Theta) =< \delta u_{\rm RD}(\Theta) >_j, \tag{3}$$

with increasing of the window size Θ, in log-log coordinates. When the window size Θ is small and increases, these functions incorporate larger structures and deviations, increasing too. The DF tends to plateau, corresponding to the SD of the whole RRLC. The RF continues increasing with decreasing rate.

Figures 1(d) and 2(d) present the DFs by dashed curves. The RFs, which pass at about 2.5 times higher ($\delta u \approx 0.4$), are considered to be less interesting and they are not shown here. All RFs are shown in all cases of Paper II. The important derivative of the RF is the rescaled RF (Eq. 5); Figs. 1(e), 2(e)). Note that the right ordinates of Fig. 1(d) and 2(d) are shown in percents.

The DF has 3 applications. First, it is used essentially for deriving of a rescaled RF. Second, the level of the DF characterizes the energy of the flickering of the QP, associated with the relevant window size Θ (Fig. 9(b)). Using the right ordinate of Fig. 1(d) for $QP = 58$ min we have $\delta u_{SD} = 7.5\%$. In Fig. 2(d) for $QP = 4.7$ min we have $\delta u_{SD} = 4\%$. Third, the initial minimum of the DF corresponds to the SD light variations on the shortest time scale, caused mainly by the photometric noise, when the window contains only 3 adjacent data points. In Figs. 1(d) and 2(d) the initial minima of the DFs are shown by horizontal segments at 3% and 3.1%. These minima of the DF in RRLCs #01–#27 occur mainly at 2.5–3%, confirming the estimation in Paper I that the electro-photometric noise is about 3%. For LCs #28–#40 the CCD noise occur mainly 0.5–1%. The ratio between the DF plateau maximum (which is the SD of the whole LC) and the minimum of the DF may be used for defining of a signal-to-noise ratio for the flickering.

The structure function (SF) of the RRLC describes the increase of a special parameter – the absolute difference between the RRLC values in the bounds of the j-th window (time lag), averaged for all k position of j window, when the window size Θ increases, in log-log coordinates. **The structure gradient (SG)** characterizes the slope of the initial quasi-linear

part of the SF. The SF and the SG are defined as follows:

$$SF_j(\Theta) =< \delta u(t+\Theta) - \delta u(t) >_j, \qquad SG = \Delta \lg (SF) \ / \ \Delta \lg \Theta. \quad (4)$$

The value of the RRLC in the boundaries of the window is derived by linear interpolation between neighboring data points.(See Paper II, Fig.4.)

Figures 1(d) and 2(d) show the SFs of the RRLCs #01 and #3a by solid curves and the SGs by solid segments. While the time lag Θ is small and increases, SF incorporates larger light variations, increases too and tends to plateau. When the lag Θ begins to include entirely one QP structure, the quantity of new larger variations decreases and the SF shows a local minimum. The SF has two applications.

First, the positions of the local minima of the SF correspond to QPs. The applying of the SF as detector of QPs is equivalent to the "phase dispersion minimization technique" of Lafler & Kinman (1965) (see Paper II and Ganchev et al. 2017, Fig. 5). If a time structure repeats, a long SF may show local minima corresponding to $2QP$ (LCs #3, #6), $3QP$ (LCs #7, #9), etc. In such cases we take into account only the basic QP, ignoring the "harmonics". Moreover, we accept QP estimation by SF only if they are confirmed by the auto-correlation function (ACF, though Fig. 1(f), 2(f)).

Occasionally we reveal "primary" (well expressed) and "secondary" (not so well expressed) QPs. In figures (d) they are marked by solid and dashed verticals, respectively. Only in the case of LC #01 (Fig. 1(d,f)) we found also a "tertiary" QP, marked by a short-dashed vertical. The values of these QPs are 11.5, 58 and 88 min. In the case of LC #03a (Fig. 2(d,f)) we found not only well expressed QP of 4.7 min, but also two shorter QPs at 3.1 and 2.5 min.

Our LCs are not suitable to reveal QPs shorter than 5 min and we ignore them. Typically, such QPs have too low amplitudes among our noisy LCs #01–#27 and the time resolution of the other LCs #28–#40 is low. Moreover, the QPs, at least the short ones, evolve by duration as in the case of RS Oph (Paper III). Note that the whole LC #01 (Fig. 1(d,f)) and 3 parts of the LC #01, presented in Appendix C, show different QPs.

The second important application of the SF concerns its SG, which contains information about the feedback of the flickering (Di Clemente et al. 1996; Kawaguchi et al. 1998). A value of $SG > 0.5$ indicates variability, driven mainly by separate shots (impulses). A value of $SG < 0.5$ corresponds to prior global flux instabilities of the FS. For example, the SGs of the dwarf nova KR Aur are below 0.35, giving a hint that so called self-organized criticality within the accretion disk may drive the shot noise continuum variability (Bachev et al, 2011). In Fig. 1(d) and Fig. 2(d)we have $SG = 0.37$ and $SG = 0.25$. Statistics of the SGs are shown in Fig. 6(a), where the median SG is 0.34 ± 0.12.

The rescaled RF, known as Hurst function (HF), describes the increasing of the ratio $RF_j \ / \ DF_j$ when the window Θ increases, in log-log coordinates. **The Hurst gradient (HG)** characterizes the slope of the advanced (at large window sizes) quasi-linear part the HF. The HF and HG are defined as follows:

$$HF_j(\Theta) =< \delta u_{RD}(\Theta)/\delta u_{SD}(\Theta) >_j, \quad HG = \Delta \lg (HF) \ / \ \Delta \lg \Theta. \quad (5)$$

Figures 1(e) and 2(e) present the HFs by dashed curves and HGs by solid segments.

Hurst (1951) asked whether fluctuations in the cumulative discharge of the Nile River scale self-similarly. He defined the rescaled RF by the full range deviation, i.e. for "peak-to-peak amplitude". In Paper II, aiming to construct a convenient illustrations we defined the RF by "the half of the peak-to-peak amplitude". By this reason our HG (Eq. 5) is smaller than the HG of Hurst by $lg2 = 0.3$. Hurst (1951) derived 0.77 for the Nile River and our value is $HG = 0.47$.

The HG has two applications. First, it characterizes the autocorrelation in the RRLC (Mandelbrot & Wallis 1968). For our definition a value of $HG < 0.2$ indicates a time series with short-term positive autocorrelation, i.e with "higher chaos". A value of $HG > 0.2$ indicates time series with long-term positive autocorrelation, i.e with "lower chaos". Second, the HG is considered as robust characterizer of apparent chaos of non-cyclic time series and robust estimator of the fractal dimension (Mandelbrot et al. 1969). The value of our HG is related to the fractal dimension for 1D process as $FD = 2 - HG - 0.3$.

In Fig. 1(e) and 2(e) the HGs are 0.11 and 0.31. The relatively low value 0.11 is connected obviously with the numerous prolonged interruptions in the LC #01. The HGs of the parts #01a, #01b and #01c of the LC #01 (Appendix C) are 0.14,.0.14 and 0.20. The 0.20 is typical for T CrB (Fig. 6(b)). Statistics of the SG and HGs are given in Fig. 6, where the median HGs is 0.18 ± 0.05.

The asymmetry function (AF) is introduced in Paper II, Eq. 10, for a time window Θ and an empiric dimensionless asymmetry parameter:

$$AF_j(\Theta) =< (\delta u_{\max} - \delta u_{\rm med}) \ / \ (\delta u_{\rm med} - \delta u_{\min}) >_j \ . \qquad (6)$$

Here $\delta u_{\rm med}$ is the median of the data in the window with size $\Theta_{\rm j}$.

Figures 1(e) and 2(e) show the AFs by solid curves. A value $AF > 0$ indicates positive asymmetry of the peaks and vise versa. Typically at large windows our AF of RRLC is positive and decreases slowly. Generally, the values of the AF are about 0.1, i.e. the ratio between the largest positive and negative deviations is roughly about 5/4. In the case of RS Oph – too.

The behavior of another AF, defined by the skewness A', is similar, but more complicated. At windows with sizes $\Theta < 5$ min, when the window contains 3–5 data points, such AF is not well defined and tends to negative values (Paper II, on-line material). This kind of AF is not shown in the present paper.

Our AF (Eq. 6) is more useful as fractal function for two reasons. First, at the short time scale, in windows containing 3–5 adjacent LC points, our AF reveals clearly a strong asymmetry of the flux changes. In such windows the flux usually grows up with increasing rate or falls down with decreasing rate (Paper II, Fig. 4(c), Fig. 10). Second, in the majority of the LCs, the AF shows well defined breakdown time-point (BT) $\Theta_{\rm BT}$. In Figs. 1(e), 2(e) and Appendices B, C the BTs are marked by verticals. About 1/8 of all AFs pose badly expressed BTs, though. Such are the LCs # # 08, 09, 10, 16, 21, 08a, 08b, 09a, 23a (Appendixes B, C). Despite that Fig. 9(a) illustrates

the usefulness of the AF as estimator of the shortest detectable QP-like light fluctuations in dependence on the time resolution of the monitoring.

Generally, our AFs give evidence that positive twinkles dominate at intermediate and short time scales in the flickering of T CrB and RS Oph.

The auto-correlation function (ACF) characterizes the change of the correlation parameter (correlation coefficient of Pearson) of the values of the RRLC on dependence of the dividing time lag (shift) τ:

$$ACF_j(\tau) =< \delta u(t+\tau) \times \delta u(t) >_j \ . \qquad (7)$$

By definition $ACF = 1$ at $\tau = 0$. In the beginning, when τ increases, the ACF decreases. It is characterized by the ACF time – the interval $\tau_{\rm ACF}$ at which the ACF takes first zero values. If the LC does not have a significant large scale trend, at larger τ the ACF fluctuates. The local positions of the maxima of the ACF correspond to QPs.

The ACF requires equally spaced data. For this reason, only for the application of ACF, every LC is resampled with step which is equal to the average resolution time $\tau_{\rm M}$ of the RRLC. Generally, the re-sampling of the LC is not recommendable. If the new step is shorter than the original one, it ignores the peaks of the LC increasing the SG and decreasing the HG.

Figures 1(f) and 2(f) show ACFs with their ACF times $\tau_{\rm ACF}$, marked by the most left verticals. The ACFs maxima that confirm the QPs, detected by the minima of the SF, are marked by verticals as for the SF in Figs. 1(d), 2(d).

2. Behavior of the flickering over the years

Basic data about the photometric behavior of the FS are collected in the on-line Appendix A, Table 1.

The observing material over 1993–2018 is divided into 3 groups (Appendix A, Table 1): (I) – 27 high speed photo-electric observations in 1993–1999 (with average 1997.1±1.4 yr), (II) – 4 CCD observations in 2009–2011 (with average 2009.7±0.4 yr) and (III) – 9 CCD observations in 2016–2018 (with average 2017.2±0.9 yr). The average years with relevant error bars are used in Fig. 3(a), 3(b) and 4(a).

In Fig. 3 the brightness variations of the FS are shown in magnitudes (U_{AV}, U_{SD}, U_RD) and in Fig. 4 – in fluxes (u_{AV}, u_{SD}, u_{RD}, Eq. 1) and residual relative fluxes (δu_{SD}, δu_{RD} Eq. 2). Figures 3 and 4(a) are based on 40 LCs. Figures 4(a) and 4(b), containing also data from 32 parts of LCs, are based on 72 LCs.

For the analysis of the graphs in Figs. 3 and 4 we remind that the number of the hundred parts of the magnitude difference, cmags, correspond well with the number of the percents of the relative flux difference in the interval 1–25 cmag or 1–25% (see for details Georgiev 2018). The formulae for conversion of small magnitude difference ΔU into relative flux $\delta u = \Delta u/u$ and vice versa are:

$$\Delta U = 2.5 \times \lg(\delta u + 1) \qquad \text{and} \qquad \delta u = \mathrm{dex}(0.4 \times \Delta U) - 1, \qquad (8)$$

for $\Delta U \geq 0$ and $\delta u \geq 0$.

In Figs. 3(a) and 4(a) the FS brightness shows minimum of $U_{AV} \approx 11$ mag in 2009.7 yr and maximum of $U_{AV} \approx 8.5$ in 2017.2 yr. The increase of the brightness U_{AV} is 2.5 mag or 10.1 times. Simultaneously, the scatter of the flickering, U_{SD} and U_{RD}, decrease from 0.06 mag to 0.03 mag and from 0.16 mag to 0.06 mag, respectively (Fig. 3(b). Therefore, with account of the increased value of u_{AV}, the values of u_{SD} and u_{RD} increase 2.7 and 3.7 times, respectively (Fig. 4(a). So, the mean increase of the flux scatter is about 3.2 time less than the increase of the average flux. Figure 3(c) shows also that the scatters U_{SD} and U_{RD} depend on the average value U_{AV} with gradients of 0.018 and 0.048, respectively.

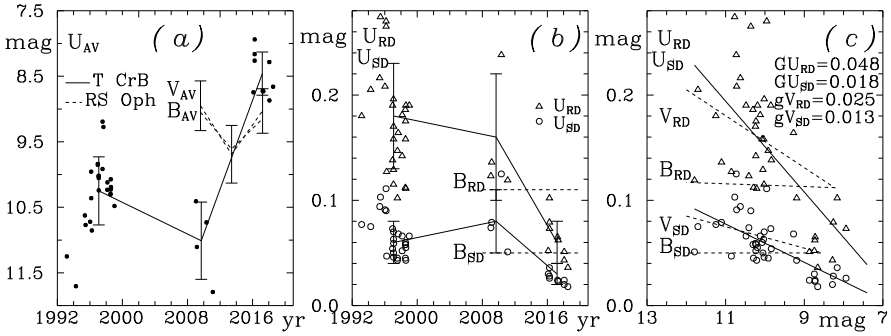

Fig. 3. (a,b): Behavior over the years of U_{AV}, U_{SD} and U_{RD} of the FS of T CrB (solid lines), as well as of the FS of RS Oph (short dashed lines). **(c):** Decreases of U_{SD} and U_{RD} with the increase of U_{AV} for C CrB in U band, as well as for RS Oph in B and $U_{SD}V$ bands. The gradients, noted by "G" and "g" correspond to T CrB and RS Oph, respectively.

For comparison, the increase of the FS V-band flux of RS Oph (Paper II) in 2015–2018 yr is 0.60 mag or 1.74 times. Then $V_{\rm SD}$ and $V_{\rm RD}$ decrease from 0.07 mag to 0.05 mag and from 0.17 mag to 0.11 mag, respectively. Therefore, $v_{\rm SD}$ and $v_{\rm RD}$ increase about 1.06 and 1.07 times, respectively. In comparison with T CrB the gradients of the flux scatter in V-band are about 1.7 times less (Fig. 3(c)). The change of B-band flux is almost the same but the values of $b_{\rm SD}$ and $b_{\rm RD}$ are almost constant, $B_{SD} \approx 0.05$ and $B_{RD} \approx 0.11$ mag. It seems the scatters B_{SD} and B_{RD} of RS Oph do not depend on the average magnitude $B_{\rm AV}$ (Fig. 3(b)), but the scatters $V_{\rm SD}$ and $V_{\rm RD}$ depends faintly on $V_{\rm AV}$ with gradients of 0.013 and 0.025, respectively (Fig. 3(c)).

Figures 4(b) and 4(c) contain data about 72 LCs (40 full and 32 partial) of T CrB. Comparison with RS Oph is given.

Figure 4(b) shows dependences of the scatters u_{SD} and $u_{\rm RD}$ on the average flux $u_{\rm AV}$. The respective dependences for RS Oph in Paper II are presented here by short dashed lines. They are a little bit more steep and narrow. The dashed line (3) with gradient 0.156 ± 0.041 presents the behav-

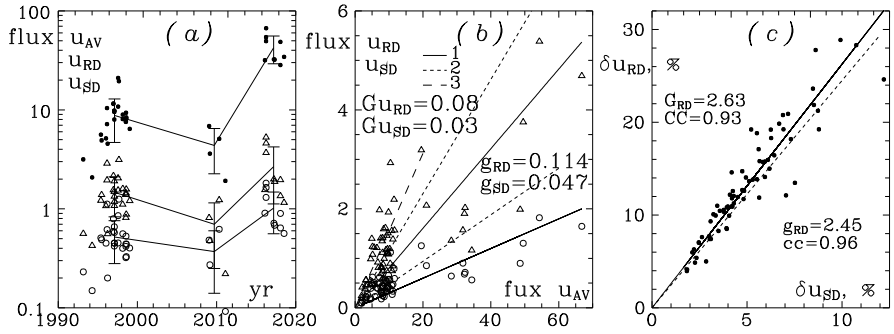

Fig. 4. (a): Behavior over the years of u_{AV} (dots), u_{RD} (triangles) and u_{SD} (circles) of the FS of T CrB. **(b):** Increase of u_{SD} (circles) and u_{RD} (triangles)with the increase of u_{AV} for T CrB in U band (1), as well as for RS Oph in B and V bands together (2). The gradients, noted by "G" and "g" correspond to T CrB and RS Oph, respectively. The steep dashed line (3) shows gradient of 0.156 ± 0.042, for u_{RD} of T CrB, found in Paper I. **(c):** Dependences between δu_{RD} and δu_{SD} for T CrB in U band (dots, solid line) and RS Oph in B and V band together (dashed line .)

ior if the parameter $F_{\rm fl} = F_{\rm AV} - F_{\rm min}$ in Paper I, Fig. 4, which practically coincides with the parameter u_{RD}. That gradient is derived on $F_{\rm AV}$ range of about 24 units and it corresponds well to the most populated left-down corner of Fig. 4(b). Our gradient, 0.080 ± 0.030, seems too low, but it is derived on $F_{\rm AV}$ range of about 65 units and it contains small number of points for average flux over 20 units. The dependence, drown by line (1) may be even parabolic, but the number of our data points is generally small.

Figure 4(c) shows narrow mutual dependence between the scatters SD and RD for T CrB, similar to that of RS Oph. These dependences have CCs > 0.9 and gradients 2.63 and 2.45, respectively. The higher gradient corresponds to the higher mean kurtosis of the flickering of T CrB in comparison with RS Oph (Fig.5(b)).

In Paper III we show that the parts of the LCs of RS Oph carry out the flickering properties of the whole LCs. In this paper we confirm this conclusion. Therefore, the scatter dependences, shown in Fig. 4(b) and 4(c) seem to be tools for comparison of very different time series.

Another comparison is also appropriate. The gradient of $u_{\rm RD}$ for RS Oph, in the B- and V- bands (Paper II, Fig. 2(b)), in range of $F_{\rm AV}$ 250 units, with flattening of the LCs, shown here in Fig.4(a), is 0.114. The respective gradient of $F_{\rm fl}$ in the $UBVRI$ system of Zamanov et al. (1915, Fig. 2), in range of $F_{\rm AV}$ 310 units, without flattening of the LCs is 0.136. Both results, derived by different data and different methods are very similar .

The regarded particularities of the flickering of T CrB give evidence that the feedbacks of the average flux and flickering are connected.

3. Statistics of the flickering parameters

Basic numerical results are collected in the Appendix A, Tables 2, 3.

The difference between the average and median values characterizes the asymmetry of the histogram (Figs. 1(c), 2(c), Appendixes B and C). In our cases these differences are close to 0, i.e. the central high populated parts of the histograms are almost symmetric. The skewness, based on the 3-rd central moment of the distribution, is more sensitive to single large deviations. (We introduce and use also an empiric asymmetry ratio, more useful as fractal indicator (Eq. 6)). The kurtosis, based on the 4-th central moment of the distribution is very sensitive to excess (or deficit) of large deviations (in respect to Gaussian distribution). The concrete skewness and kurtosis depend on the goodness of the removal of the large scale trend (Sect. 1.1) and must be analyzed statistically, for numerous RRLCs (Figs. 5 and 6).

Figure 5 compares the distributions of the skewness A' and the kurtosis E' of histograms of LCs – 72 of T CrB (this work) and 58 of RS Oph (Paper II, Fig. 3). The respective median values and median deviations for RS Oph are 0.08 ± 0.26 and -0.17 ± 0.63. For T CrB they are 0.24 ± 0.32 and 0.02 ± 0.44, higher by factor of 0.16 and 0.19, respectively. The average skewness of T CrB is more positive, i.e. the flickering contains larger amount of positive shots (Fig. 5(a)). Also, the average kurtosis of T CrB is almost zero, close by its central part to Gaussian distribution. Therefore, in contrast with RS Oph the flickering of T CrB contains enough amount of short deviations from the mean value (from the polynomial fit). The CC between A' and E' is 0.32 for T CrB and 0.43 for RS Oph. In both cases the values of A' and E' have negligible correlation.

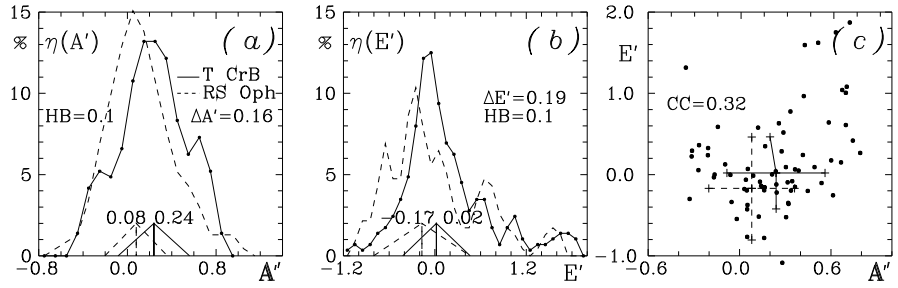

Fig. 5. (**a,b**): Distributions of the skewness A' and the kurtosis E' of the RRLC of T CrB and RS Oph. The apex and the base of the triangle below the distribution show the median value and the median error bar, containing 68% of the data (see Figs. 1(c) and 2(c)); (**c**): Mutual distribution of A' and E' for T CrB. Crosses present the medians and median error bars of T CrB (here) and RS Oph (Paper II, Fig. 3(c)).

Figure 6 compares the distributions of the the SG (Eq. 4) and the HG (Eq. 5) for 72 LCs of T CrB (this work) and 58 LCs for RS Oph (Paper II, Fig.8). The median values for RS Oph are 0.48 ± 0.19 and 0.21 ± 0.06. The median values for T CrB are 0.34 ± 0.12 and 0.18 ± 0.05, respectively, less by 0.14 and 0.03. The median SG of the LCs of T CrB is significantly less than

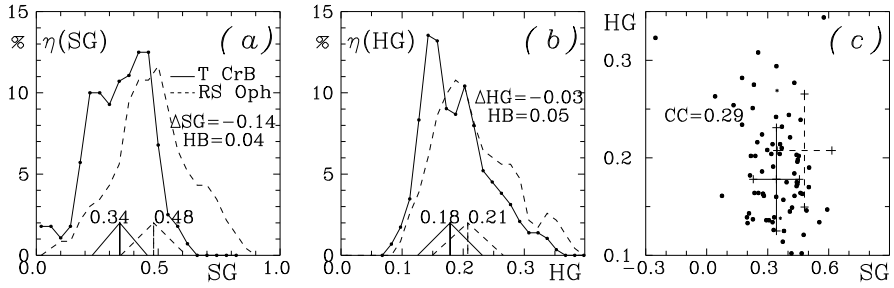

Fig. 6. (**a,b**): Distributions of the structure gradient SG and Hurst gradient HG for the RRLCs of T CrB and RS Oph. Triangles show the median values and median error bars, covering 68% of the data (see Fig. 1(c) and 2(c)); (**c**): Mutual distribution of SG and HG for T CrB. Crosses present the median error bars for T CrB (here) and RS Oph (Paper II, Fig. 6(c))

the limit 0.5. Therefore, the flickering of T CrB contains less contribution of shots (twinkles) than RS Oph. The median HG of the LCs of T CrB is a little less than the limit 0.2, i.e. the flickering of T CrB poses shorter autocorrelations. The CC between the SGs and HGs of T CrB, $CC = 0.29$, is negligible. In the case of RS Oph we had $CC = 0.2$,which is lower. The values of SG and HG seem to be mutually independent. The mean fractal dimension of the LCs is 1.52 ± 0.05 for T CrB, 1.48 ± 0.06 for RS Oph, and 1.5 for Gaussian distribution.

Generally, in the multi-minute flickering of of T CrB the distributions of A' and E', (Fig. 5), as well as these of SG and HG (Fig. 6) are similar to these of RS Oph and not very different from a Gaussian. The differences are in the frames of the statistical errors. Though, in comparison with Gaussian, T CrB shows some excess of large positive shots and RS Oph shows some deficit of short deviations.

4. Quasi-periods of the flickering and their modes

Basic numerical results are collected in the Appendix A, Table 4.

As in the case of RS Oph, the detectability of the QPs in the case of T CrB depends on the observing circumstances – monitoring time $T_{\rm M}$, resolution time $\tau_{\rm M}$ and autocorrelation time $T_{\rm ACF}$. In this sense the detectability in the case of T CrB is just the same as in the case of RS Oph and it is not illustrated here again. Our QPs have $QP < T_{\rm M}$, $QP > 5 \times \tau_{\rm M}$ and $QP > \tau_{\rm ACF}$, as in Paper II, Fig. 14.

In Paper III, Fig. 3, we established the regularity (near-commensurability) of the distribution of 8 QP modes of RS Oph, found in Paper II and Paper III. The QP modes occur at 3.5, 5.3, 8, 13, 21, 30, 48 and 73 min, following the power function:

$$QP_M = 3.47 \times 1.55^M \qquad \text{or} \qquad \lg QP = 0.54 + 0.19 \times M. \tag{9}$$

Here M is the mode number where $M = 0$ is chosen for $QP = 3.5$ min. Note that $1.55 \approx 3/2$. The difference $1.55 - 3/2 = 0.05$, overcomes weakly

the 90% Student's criterion of confidence and this is a hint for a possible 3:2 resonance with unknown nature.

In Paper III, Fig. 4, we demonstrated also some evolutions of the QP modes of RS Oph in the minute scale, including jumps from one mean QP to another. We evidence that such changes of QPs modes exist also in the flickering of T CrB, on the minute scale and on the multi-minute scale. The flickering of T CrB posses higher noise (because of the domination of the photo-electric observations), but posses naturally lower light variations.

In the present case of T CrB we found 84 QPs (Appendix A, Table 4). They are detected by the minima of SFs (Eq. 4) and confirmed by the maxima of ACFs (Eq. 7). Among them 48 QPs are found in 40 whole initial LCs and 36 QPs are revealed in 32 parts of these LCs (Appendix B and C).

Figures 7(a) and 7(b) present the distributions of the QPs over linear time scale and over logarithmic time scale, respectively. The regularity of the distribution of 84 QPs in 5 QP modes, at 4.7, 11.8, 19.0, 42.1 and 81.7 min, is established. These modes follow the power function:

$$QP_M = 5.1 \times 2.0^M \qquad \text{or} \qquad \lg QP = 0.7 + 0.3 \times M. \tag{10}$$

The mode number $M = 0$ is chosen for about $QP = 5$ min. The best expressed mode is $M = 2$ at $QP \approx 20$ min.

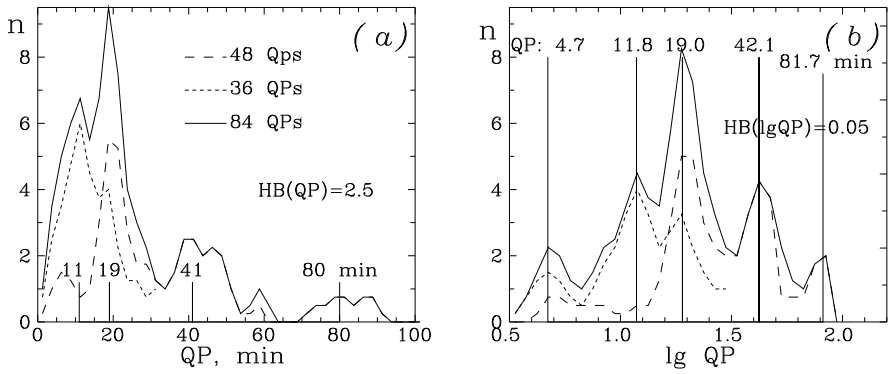

Fig. 7. Joint distribution of the QPs of T CrB over linear time scale **(a)** and over logarithmic time scale **(b)**. The revealed 5 QP modes are marked by vertical segments.

Figure 8 shows the major difference between the flickering of the FSs of T CrB and RS Oph. In contrast with the case of RS Oph, where the modes follow like a 3:2 resonance, the QP modes of T CrB like follow 2:1 resonance. Note that at RS Oph and T CrB we ignore the QPs of the type $2QP$, $3QP$ etc., if they belong in a single LC together with the primary QP. The mentioned "resonances" are revealed by independent single QPs.

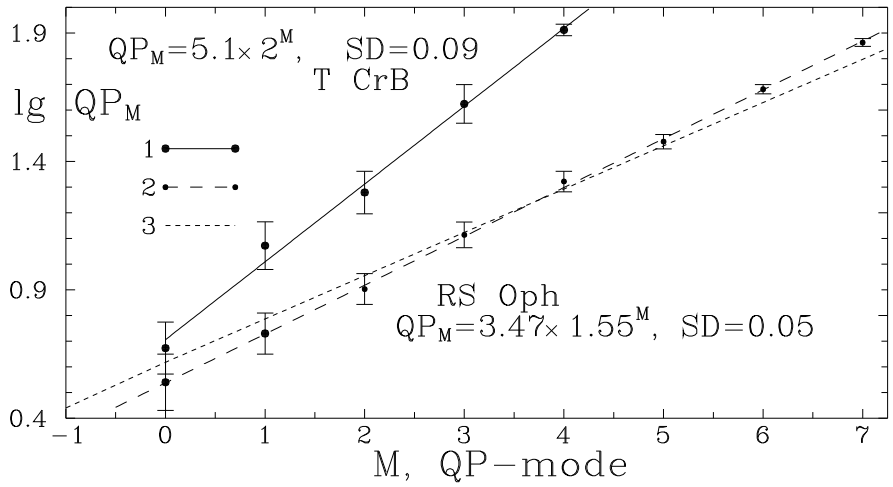

Fig. 8. Regularity of 5 QP modes of T CrB along the power function Eq. 10 (solid line, top formulas) and regularity of 8 QP modes of RS Oph along the power function ib Eq. 9 (solid line, bottom formulas). The close power function with base 1.5=3/2 (dashed line) is build though the mode of 21 min.

5. The shortest twinkles and the energies of the quasi-periods

The FSs of T CrB ought to be characterized and compared with RS Oph also by two other dependences.

In Paper II, Fig. 11, we found exponential dependence of the BT, $\Theta_{\rm BT}$, on the AF (Eq. 6 in this paper) on the resolution time of the monitoring $\tau_{\rm M}$. The intercept, estimated to be $\tau_0/2 = 1.8 \pm 0.8$ min, was interpreted as the half-time of the shortest discernable shots in the LC. Thus, the full duration of these shots for RS Oph is estimated to be $\tau_0 = 3.6 \pm 0.8$ min.

Figure 9(a) shows the dependence of BT on the time resolution $\tau_{\rm M}$ of the LC for all 72 RRLCs of T CrB (dots, Line 1, linear regression). This dependence has remarkable high correlation coefficient, $CC = 0.99$. It includes high-resolution electro-photometric observations and it reaches $\tau_0/2 = 0.6$. However, our 13 CCD LCs with low time resolution(exponential curve (2)) show intercept point about 2.5 min, estimating the duration of the shortest discernable shots to be about 5 min. The exponential curve (3) corresponds to RS Oph. The present data about T CrB give evidence of the presence of QPs with durations about 2.5 min, as in Fig. 2. The shortest QPs (if they exists) may be studied in the future by high time resolution LCs.

Figure 9(b) presents the approximative proportionality between the QP and its relevant DF level, found for T CrB (this paper) and RS Oph (Paper III). Line (1) corresponds to 74 QPs from the LCs #01–#31, in the low stare of T CrB, before 2016. Among them 38 (circles) are found in the whole

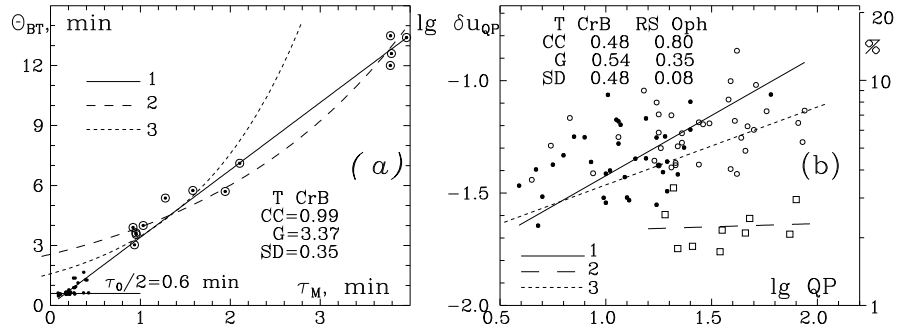

Fig. 9. (a): Dependence of the breakdown time $\Theta_{\rm Bt}$ of the AF on the time resolution $\tau_{\rm M}$ of the LC. (1) – for all 72 LCs of T CrB; (2) – for 13 CCD LCs of T CrB; (3) – for RS Oph. CC is correlation coefficient, G is regression gradient (slope coefficient) and SD is the regression standard deviation for line (1). **(b)**: Regression dependences between the quasi-period QP and the relevant level of the density function DF δu_{QP}: (1) for 74 QPs from the low state of T CrB, before 2016, (circles and dots), (2) for 10 QPs in the high state of T CrB, in 2016–2017; (3) for RS Oph in Paper III. Lines (1) and (3) are the bisectors of the relevant ordinary and reverse regressions.

LCs and 36 (dots) – in the partial LCs. Line (2) corresponds to 10 QPs (squares) from LCs #32–#40, in the high stare of T CrB in 2016–2018. These QPs obviously are representatives of another LC population. Line (3) is the regression for RS Oph in Paper III, Fig. 5(b), build by 168 QPs.

Figure 9(b) shows that in comparison with RS Oph, the FS of T CrB in low state corresponds to higher DF levels and poses higher gradient of the dependence. It seems that these facts are due to the higher photometric noise of the majority of the T CrB observations. It seems the approximative proportionality between the QP and relevant DF level (Fig, 8(b)) may be tools for comparison of the powers of flickering processes.

The analysis of the QPs in the LCs and parts of the LCs of T CrB again do not answer clearly the first question about the dominating feedback of the flickering – local shots of global disk instabilities. Obviously, the flickering phenomenon is very complicated in all its manifestations.

Conclusions

We applied a system of statistical and fractal tools to characterize the light curves and quasi-periods of the flickering source in T CrB by studying 40 LCs in U-band over the years 1993–2018. The method (Figs. 1, 2, Appendices B, C), developed in Paper II for RS Oph is entirely applicable to T CrB too. The main results follow.

1. The photometric diagrams (Fig. 3, Fig. 4) show that in 2009–2017 the AV flux of the FS has increased 10.1 times, while the SD and RD have increased 2.7 and 3.7 times, less of about 3 times. In the case of RS Oph, for only 1.7 times increase of the AV flux in 2015–2017, the SD and RD in stay

almost unchanged (Fig. 3(b); Paper II, Fig. 2). Therefore, the feedbacks of the AV flux and flickering SD or RD are connected.

2. The distributions of the skewness and kurtosis (Fig. 5), as well as of the SG and HG (Fig. 6) of T CrB are similar to these of RS Oph (Paper II). The differences between their averages lie in the frames of the statistical errors. In comparison with a Gaussian, T CrB shows some excess of large deviations and RS Oph shows some deficit of small deviation. It seems the single local shots are present in the flickering of T CrB with some privilege.

3. All flickering LCs posses QPs and the Qp of about 19 min is the most spread. The QP and the relevant level of the DF $\delta u_{\rm QP}$ posses moderate correlation (Fig. 9(b)). The distribution of the revealed 84 QPs shows 5 modes, placed at 4.7, 11.8, 19.0, 42.1 and 81.7 min (Fig. 7, 8). These QP modes follow a power function with degree 2 and SD of 9%, while 8 QP modes in the case of RS Oph is $1.55 \approx 3/2$ with SD of 5% (Paper III). These different power functions are the main difference between the flickering of RS Oph and T CrB. They describes regularities as resonances 3:2 and 2:1 with unknown reasons.

4. Our empiric AF (Eq. 6, Fig. 1(e), 2(e)), introduced in Paper II, gives evidence that the positive twinkles in the flickering of T CrB and RS Oph dominate at short time scales. The contribution of these twinkles decreases gradually toward large time scale. This AF shows also that the duration of the shortest positive shots is about 1.2 min (Fig. 9(a)). The distribution of the QP modes (Fig. 8) predicts mode at 2.5 min, which is not detected in this work. However, it coincides with the elementary shot with duration about 2.4 min (2×1.2 min).

5. The relationships between AV flux and SD or RD of the flickering seem to be universal and suitable for general comparison of flickering time series. The results in this paper and in other papers, derived by different methods are very close (Fig. 4(b)). Such dependences are found e.g. for cataclysmic variables MV Lyr (Scaringi et al. 2012), V1504 Cyg and KIC 8751494 (Van de Sande et al. 2015). Amplitude–flux relation in log-log coordinates for T CrB and RS Oph with gradients ≈ 1 are found in Paper I and by Zamanov et al. (2015), respectively. Such relationships are known also for massive accretion disks, e. g. in CH Cyg (Mikołajewski et al. 1990) and MWC 560 (Tomov et al. 1996).

Acknowledgments: This work is supported by the grant КП-06-H28/2 08.12.2018 (Bulgarian National Science Fund).

The authors are especially grateful to the anonymous referee for their attention to this paper and numerous recommendations.

References

Bachev, R., Boeva, S., Georgievm Ts., Latev, G., Spassov, B., Stoyanov, K., Tsvetkova, S. 2011, Bulg. Astron. J., 16, 31
Bessel, M. S. 1979, PASP, 91, 589
di Clemente, A., Giallongo, E., Natali, G., Trevese, D., Vagnetti, F. 1996, ApJ, 463, 466
Falconer K. 1997, *Techniques in Fractal Geometry*, John Willey & Sons
Fekel, F. C., Joyce, R. R.; Hinkle, K. H., Skrutskie, M. F. 2000, AJ, 119 (3), 1375
Gantchev, G., Valcheva, A., Nedialkov, P., Ovcharov, E. 2017, Bulg. Astron. J., 26, 16

Georgiev, T.B. 2018, Publ. Astron. Soc. Bulgaria, 2018, 1, http://astro.shu-bg.net/pasb/
Georgiev, T., Zamanov, R., Boeva, S., Latev, G., Spassov, B., Martí, J., Nikolov, G., Ibryamov, S., Tsvetkova, S., Stoyanov, K. A. 2020, Bulg. Astron. J., 32, p.35 (Paper II)
Georgiev, T., Zamanov, R., Boeva, S., Latev, G., Spassov, B., Martí, J., Nikolov, G., Ibryamov, S., Tsvetkova, S., Stoyanov, K. A. 2020, Bulg. Astron. J., 33, p.3 (Paper III)
Hastings H. M., Sugihara G. 1995, *Fractals. A user guide for Natural Sciences*, Oxford University Press.
Hurst, H.E. 1951, Transactions of American Society of Civil Engineers. 116: 77
Iłkiewicz, T., Mikołajewska, J., Stoyanov, K., Manousakis, A., Miszalski, B. 2016, MNRAS, 462 (3), 2695
Joanes, D. N., Gill, C. A. 1998, Journal of the Royal Statistical Society, Series D., 47 (1), 183?18
Kawaguchi, K., Mineshige, S., Umemura, M., Turner, E. L. 1998, ApJ 504, 671
Lafler, J., & Kinman, T.D. 1965, ApJS 11, 216
Mandelbrot B. B. 1982, *The fractal Geometry of Nature*, Freeman, New York
Mandelbrot, B. B., Wallis, J. R. 1968, Water Resources Research, 4, 90991
Mandelbrot, B. B., Wallis, J.R. 1969, Water Resources Research, 5 (5), 967988
Mikołajewski, M., Mikołajewska, J., Hpmpv, T., Kulesza, B., Szczerba R. 1990, Acta Astronomica 40, 129
Russ J.C. 1994, *Fractal Surfaces*, Plenum Press, New York & London
Scaringi, S., Körding, E., Uttley, P., et al. 2012, MNRAS. 448, 2430
Shenavrin, V. I., Taranova, O. G., Nadzhip, A. E. 2011, Astronomy Reports, 55, 31
Tomov, T.; Kolev, D.; Ivanov, M.; Antov, A.; Jones, A.; Mikolajewski, M.; Lepardo, A.; Passuello, R.; Saccavino, S.; Sostero, G.; Valentinuzzi, T.; Bellas-Velidis, Y.; Dapergolas, A.; Munari, U. 1996, A&AS, 116, 1
Van de Sande, M., Scaringi, S., Knigge, C. 2015, MNRAS, 448, 2430
Stanishev, V., Zamanov, R., Tomov, N., Marziani, P. 2004, A&A, 415 (2), 609
Zamanov, R., Bode, M. F., Stanishev, V., Martí, J. 2004,MNRAS 350, 1477. (Paper I)
Zamanov, R., Latev, G., Boeva, S., Sokoloski, J. L., Stoyanov, K., Bachev, R., Spassov, B., Nikolov, G., Golev , V., Ibryamov, S. 2015,MNRAS, 450, 3958